Japanese Journal of Applied Physics **62**, SD1010 (2023)
https://doi.org/10.35848/1347-4065/aca4d7 **REGULAR PAPER**

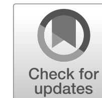

Towards B-doped p-$BaSi_2$ films on Si substrates by co-sputtering of $BaSi_2$, Ba, and B-doped Si targets

Hayato Hasebe[1], Kazuki Kido[1], Haruki Takenaka[1], Masami Mesuda[2], Kaoru Toko[3], Dmitri B. Migas[4,5], and Takashi Suemasu[3*]

[1]*Degree programs in Pure and Applied Sciences, Graduate School of Science and Technology, University of Tsukuba, Tsukuba, Ibaraki 305-8573, Japan*
[2]*Tosoh Corporation, Advanced Materials Research Laboratory, Ayase, Kanagawa 252-1123, Japan*
[3]*Department of Applied Physics, Faculty of Pure and Applied Sciences, University of Tsukuba, Tsukuba, Ibaraki 305-8573, Japan*
[4]*Belarusian State University of Informatics and Radioelectronics, P. Brovki 6, 220013 Minsk, Belarus*
[5]*National Research Nuclear University MEPhI (Moscow Engineering Physics Institute), Kashirskoe Shosse 31, 115409 Moscow, Russia*

[*]E-mail: suemasu.takashi.gu@u.tsukuba.ac.jp

Received September 23, 2022; revised October 22, 2022; accepted November 21, 2022; published online December 20, 2022

$BaSi_2$ is one of the emerging materials for thin-film solar cell applications; hence the conductivity control by impurity doping is of great importance. The formation of B-doped p-$BaSi_2$ films has been achieved by molecular beam epitaxy and vacuum evaporation. We fabricated B-doped $BaSi_2$ films on Si substrates at 600 °C by co-sputtering $BaSi_2$, Ba, and B-doped Si targets, followed by post-annealing at 900 °C or 1000 °C for 5 min in an Ar atmosphere. Contrary to expectations, as-grown sample and the sample annealed at 900 °C showed n-type conductivity, while the sample annealed at 1000 °C showed p-type conductivity. The reason for the n-type conductivity was discussed based on first-principles calculation considering the presence of oxygen atoms in the order of 10^{21} cm^{-3}. The n-type conductivity for B-doped $BaSi_2$ is possible only when both the B and O atoms being a substitution impurity are in the same Si_4 tetrahedron. © 2022 The Japan Society of Applied Physics

1. Introduction

Currently, the majority of solar cells in the market is made from wafer-based crystalline Si (c-Si), and the conversion efficiency of c-Si solar cells exceeded 26%.[1] However, the installation of c-Si solar panels is limited to rooftops and other flat areas. To further deploy the solar panels to achieve a decarbonized society, thin-film solar cells are of particular importance. There have been lots of studies on thin-film solar cell materials with high absorption coefficients such as chalcopyrite, CdTe, and perovskite thus far.[2–12] However, they contain nonabundant and/or toxic elements. Under such circumstances, semiconducting barium disilicide ($BaSi_2$) has drawn increasing attention.[13–16] $BaSi_2$ is composed of Earth-abundant Ba and Si, and has a band gap of 1.3 eV,[17] close to the ideal value for solar cells.[18] The most attractive feature of $BaSi_2$ is its high absorption coefficient[19] in spite of an indirect transition semiconductor, caused by a large matrix element across the band gap.[20,21] In addition, bipolar doping is possible.[14,22] Thus far, various types of $BaSi_2$ solar cells have been proposed[13,23–28] and fabricated in the form of $BaSi_2$/Si,[29–32] $BaSi_2$-pn,[33] and n-ZnO/p-$BaSi_2$,[34,35] and SnS/$BaSi_2$[36] by thin-film growth methos such as molecular beam epitaxy, sputtering, and vacuum evaporation. For large-area deposition of $BaSi_2$ thin-films, vacuum evaporation and sputtering have been developed.[31,36–49]

The control of carrier type and carrier concentration of $BaSi_2$ by impurity doping is very important for device applications. Thus far, the formation of B-doped p-$BaSi_2$ films has been achieved by molecular beam epitaxy,[50,51] and vacuum evaporation,[32,52,53] and ion implantation;[54,55] however, there have been no reports on sputter-deposited impurity-doped $BaSi_2$. In this work, we aim to form B-doped p-$BaSi_2$ films by sputtering. As for the formation of impurity-doped semiconducting films by sputtering, ZnO and Al_2O_3 targets are employed to form Al-doped n-ZnO films by sputtering.[56–58] This is to avoid the reaction of the Al target with O_2 to form Al oxides, leading to a sudden change in sputtering rate during deposition. For the formation of As-doped p-ZnO films by sputtering, ZnO and Zn_3As_2 targets are used.[59]

2. Experiment

2.1. Formation and characterizations of $BaSi_2$ films

We used a 2-inch diameter polycrystalline stoichiometric $BaSi_2$ target, a 1-inch diameter Ba target, and a 2-inch diameter B-doped Si target. The $BaSi_2$ target was manufactured by Tosoh Corporation. B-doped $BaSi_2$ films were fabricated on floating-zone n-Si(111) substrates (resistivity $\rho > 1000\ \Omega$ cm) by a helicon wave plasma sputtering system (ULVAC MB00-1040). The substrate temperature was set at 600 °C during deposition. The Ar pressure was set at 0.5 Pa. The radio-frequency (RF) power of the $BaSi_2$ target, Ba target, and B-doped Si target was set at 70 W, 40 W, and 50 W respectively. Subsequently, 3 nm thick a-Si was deposited on each sample to prevent oxidation of the B-doped $BaSi_2$ films.[60] The B concentration of the grown sample was 1×10^{18} cm^{-3}. As described later, since the as-grown samples were n-type, post-annealing was performed in an Ar atmosphere using a rapid-thermal annealing system (ULVAC MILA-5000UHV). For comparison, we also prepared B-doped $BaSi_2$ films by MBE. To prevent oxidation of the samples, two samples were put face-to-face, and surrounded by several sacrificial $BaSi_2$/Si samples.[61] In the post-annealing, pre-annealing was conducted at 200 °C for 30 min to eliminate moisture in the furnace, followed by the main annealing for 5 min at temperatures (T_a) at 900 °C or 1000 °C. The heat-up and cool-down rates of the furnace temperature was set at 5 °C s^{-1}. After post-annealing, 150 nm thick Al electrodes with a diameter of 1 mm were deposited on the sample surface for hole measurement using an RF magnetron sputtering system. The crystalline quality was evaluated by grazing-incidence (GI) x-ray diffraction (XRD: Rigaku Smart Lab) using a Cu Kα radiation source and a Raman spectroscopy (JASCO NRS- 5100) with a frequency-doubled Nd:YAG laser ($\lambda = 532$ nm, 5.1 mW).

 © 2022 The Japan Society of Applied Physics

The incident angle of x-rays was 0.4° from the sample plane to enhance the penetration depth in the $BaSi_2$ films x-rays travel. In addition, Hall measurements using the Van der Pauw method were conducted for electrical characterization. Depth profiles of B and O atoms were evaluated by secondary ion mass spectrometry (SIMS) measurements using Cs^+ ions. For the SIMS measurements, standard samples for B and O atoms in $BaSi_2$ were fabricated for quantitative evaluation. x-ray photoelectron spectroscopy (XPS: JEOL, JPS-9010) measurements were also conducted to investigate the bonding state of atoms in the depth direction.

2.2. Computational details

In order to detect the conductivity type and to trace the appearance of localized states in the gap of $BaSi_2$ doped with O and B atoms we utilized the first-principles total energy projector-augmented wave method (VASP code).[62–64] The full structural optimization (i.e. lattice parameters and atomic positions) was first performed, followed by calculations of the density of states. We used a $2 \times 3 \times 2$ increased unit cell of $BaSi_2$, where one of its structural peculiarities was the formation of Si_4 tetrahedra,[65] to avoid relatively strong defect-defect interaction. For the exchange and correlation potentials the generalized gradient approximation of Perdew–Burke–Ernzerhof[66] was implemented. The energy cutoff was set at 400 eV, which was sufficient to ensure total energy convergence within a few meV per cell. For the Brillouin zone integration, a $5 \times 5 \times 5$ mesh of Monkhorst–Pack points was used. Further increase in the k-point mesh did not lead to a change in the total energy of more than 0.001 eV per cell. The atomic relaxation was stopped when forces on the atoms were smaller than 0.05 eV Å^{-1}. The total DOS was calculated by the tetrahedron method with Blöchl corrections.

3. Result and discussion

The Raman spectra of samples are shown in Fig. 1(a). For all of the samples, A_g, E_g, and F_g peaks were observed, which originate from the vibrational modes of the Si tetrahedra in the lattice of $BaSi_2$,[67] and it was confirmed that the $BaSi_2$ crystallized. Regarding the Raman spectra of the post-annealed samples, the full-width at half maximum (FWHM) of the A_g mode peak was 12.3 and 11.8 cm^{-1} at $T_a = 900$ and 1000 °C, respectively. These values are smaller than 15.7 cm^{-1} for the as-grown sample, suggesting that the crystalline quality of the post-annealed samples has improved.

Figure 1(b) shows the GI-XRD patterns of the samples. For comparison, the calculated powder diffraction pattern of orthorhombic $BaSi_2$ is also shown. All of the obtained peaks were assigned to $BaSi_2$, suggesting that randomly oriented polycrystalline $BaSi_2$ films were formed for the as-grown sample and the sample annealed at $T_a = 900$ °C. When the T_a was increased to 1000 °C, the XRD pattern changed drastically, and 301 and 402 reflections of $BaSi_2$ became dominant. This means that the migration of Ba and/or Si atoms was promoted at temperatures higher than somewhere between 900 °C and 1000 °C. This result is different from those obtained for *a*-axis-oriented $BaSi_2$ epitaxial films,[68] wherein *a*-axis crystal orientation started to degrade sharply at $T_a \geqslant 800$ °C, and there was not much difference in the FWHM of XRD $BaSi_2$ 600 peak as well as photoresponsivity of samples annealed at between 900 °C and 1000 °C. This result suggests that the migration of atoms is less likely to occur in the sputter-deposited $BaSi_2$ polycrystalline films than that in *a*-axis-oriented $BaSi_2$ epitaxial films.

Figure 2 shows the optical microscopy images of samples. For post-annealed samples, cracks were observed on the surface. We speculate that a much higher thermal expansion coefficient of $BaSi_2$ than that of c-Si might induce these cracks. The Young's modulus and Poisson's ratio are reported to be 50 GPa and 0.201 for $BaSi_2$, respectively.[69] $BaSi_2$ films might expand during the high-temperature annealing, and shrink at the cooling process, generating cracks.

Figure 3 shows the carrier concentration and carrier mobility of the samples. For comparison, the post-annealing

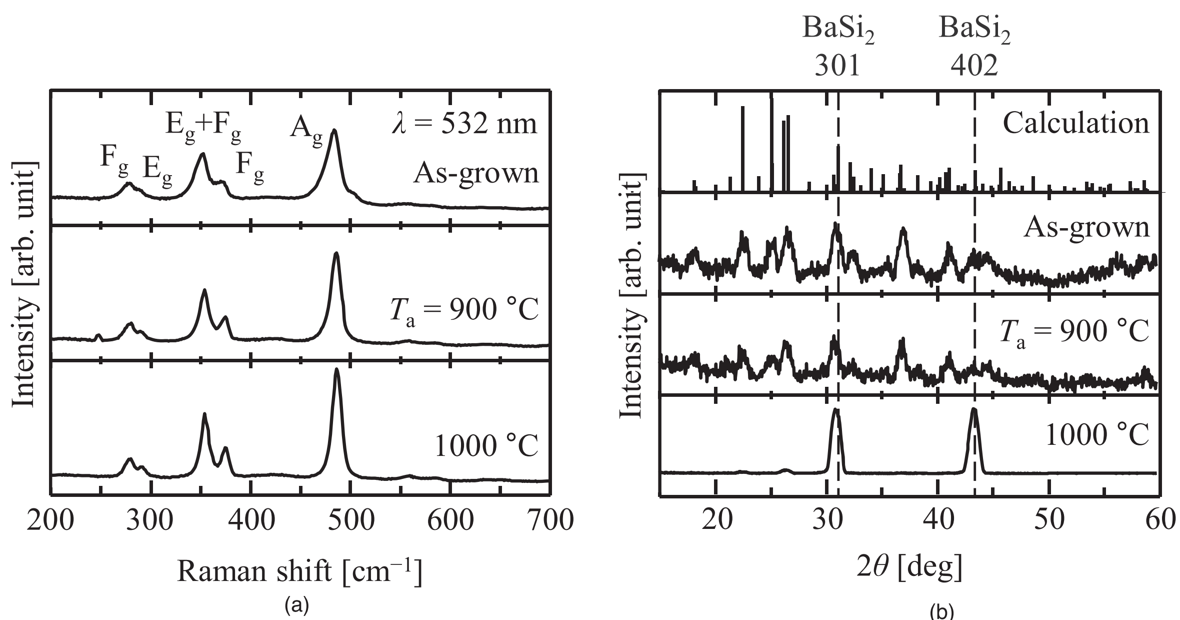

Fig. 1. (a) Raman spectra of B-doped $BaSi_2$. The peaks denoted by A_g, E_g, and F_g originate from the vibrational modes of the Si tetrahedra in the lattice of $BaSi_2$. (b) GI-XRD patterns of B-doped $BaSi_2$.

© 2022 The Japan Society of Applied Physics

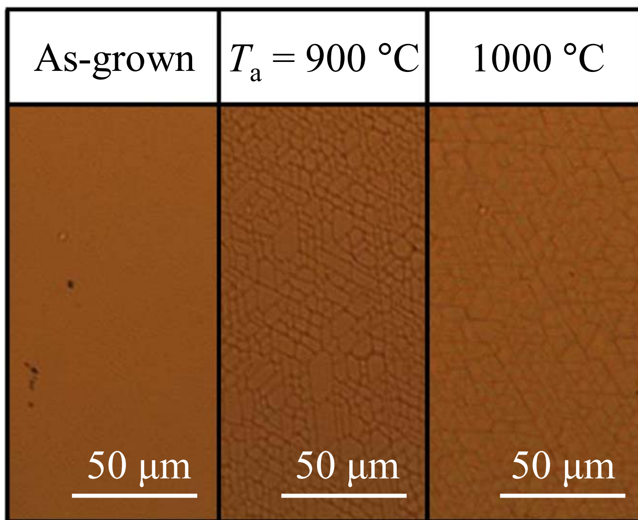

Fig. 2. (Color online) Optical microscopy images of B-doped $BaSi_2$ samples.

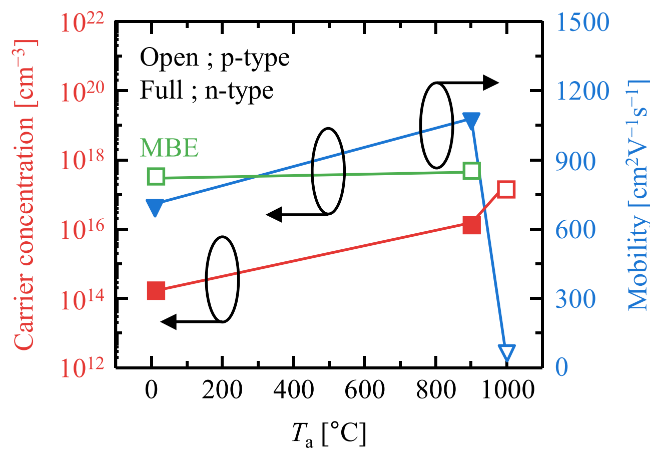

Fig. 3. (Color online) Carrier concentration and carrier mobility of B-doped $BaSi_2$ films fabricated by sputtering and by MBE.[70]

effect on the hole concentration of B-doped p-$BaSi_2$ epitaxial films grown by molecular beam epitaxy (MBE) is shown.[70] The hole concentration of p-$BaSi_2$ films by MBE remained almost unchanged in the range $p = 3$–4×10^{17} cm^{-3} even after the post-annealing at $T_a = 900$ °C.[70] As for the sputter-deposited samples, however, the as-grown sample and the post-annealed sample at T_a = 900 °C showed n-type conductivity with an electron concentration in the range 10^{14}–10^{16} cm^{-3}. In contrast, the post-annealed sample at T_a = 1000 °C showed p-type conductivity with $p = 2.1 \times 10^{17}$ cm^{-3} and a hole mobility of 40 cm^2 V^{-1} s^{-1}. Since the top of the valence band maximum of $BaSi_2$ mainly consists of Si p states, the replacement of some of Si atoms in $BaSi_2$ by group 13 elements like B form p-type $BaSi_2$.[20,21,71] Considering that the drastic change in GI-XRD pattern observed for this sample in Fig. 1(b), it is considered that the activation of B occurred by the diffusion and substitution of B atoms for Si sites.

We next discuss the origin of n-type conductivity of sputter-deposited $BaSi_2$ films. It is noted that even B-doped $BaSi_2$ epitaxial films grown by MBE show n-type conductivity when the Ba/Si ratio in the $BaSi_2$ films departs from stoichiometry.[72] In this work, we explore another possibility, which is the effect of O atoms in $BaSi_2$. Figure 4 shows the depth profiles of B and O atoms, and (Ba + Si) ion intensity in the as-grown samples fabricated by (a) sputtering and by (b) MBE. The B concentration was 1×10^{18} cm^{-3} for the sputter-deposited sample and 1×10^{18} cm^{-3} in the MBE-grown sample. To our surprise, the O concentration differed by three orders of magnitude between them: it was as much as 5.0×10^{21} cm^{-3} and 4.0×10^{18} cm^{-3}, respectively.

Figure 5 shows the depth-dependent Si 2 s core-level XPS spectra of the sputter-deposited as-grown sample. The etching duration (t_{etch}) was varied from 12 to 372 s. At t_{etch} = 6 s, the capping layers were completely etched, and the $BaSi_2$ films remained at t_{etch} = 372 s. The peaks were normalized to the peak intensity of the Si 2 s orbitals at around 148.5 eV. At the left shoulder of the Si 2 s orbital, a peak indicating the presence of oxidized Si was detected. These results mean that the O atoms in $BaSi_2$ films formed bonding with Si atoms.

Since there is such a high concentration of O atoms in our samples, as a first step we have carefully checked the influence of an O atom being both a substitution and interstitial impurity on electronic properties of $BaSi_2$. The concentration of O impurities in the increased unit cell of $BaSi_2$ under consideration is about 1.2×10^{20} cm^{-3}. Previously the effect of O doping of $BaSi_2$ was investigated by us primarily as a possibility to tune the band gap value and shift the absorption edge via changes in the lattice parameters[73] without going into detail on a possible appearance of localized states in the gap. Thus, depending on a number of first neighbors and the corresponding interatomic

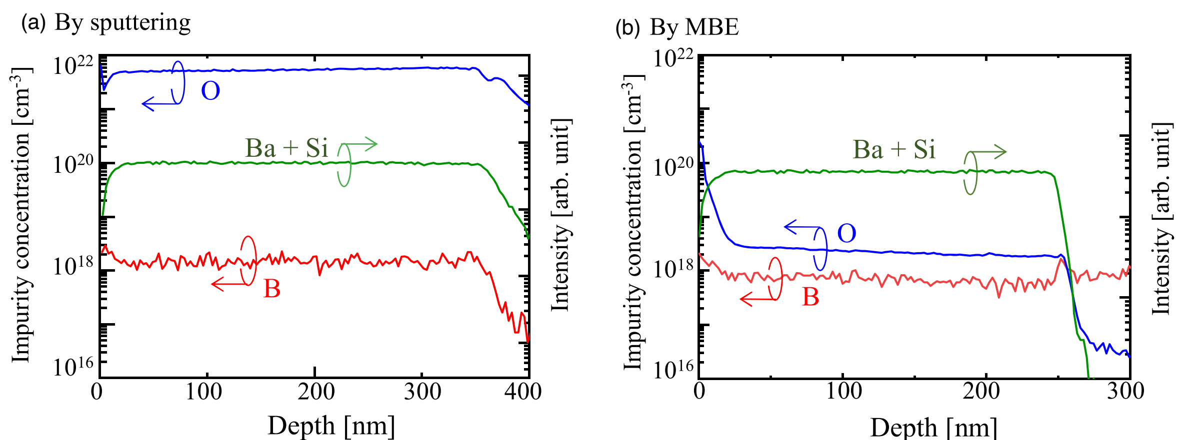

Fig. 4. (Color online) SIMS depth profiles of B and O concentrations and secondary ions (Ba + Si) of $BaSi_2$ films fabricated by (a) sputtering and (b) MBE.

© 2022 The Japan Society of Applied Physics

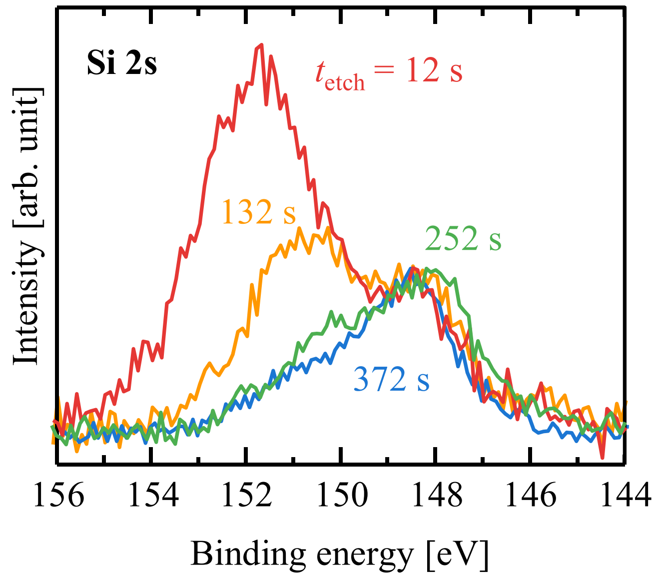

Fig. 5. (Color online) Etching duration (t_{etch})-dependent normalized Si 2 s core-level XPS spectra of the sputter-deposited as-grown sample. The in situ etching duration (t_{etch}) was varied from 12 to 372 s.

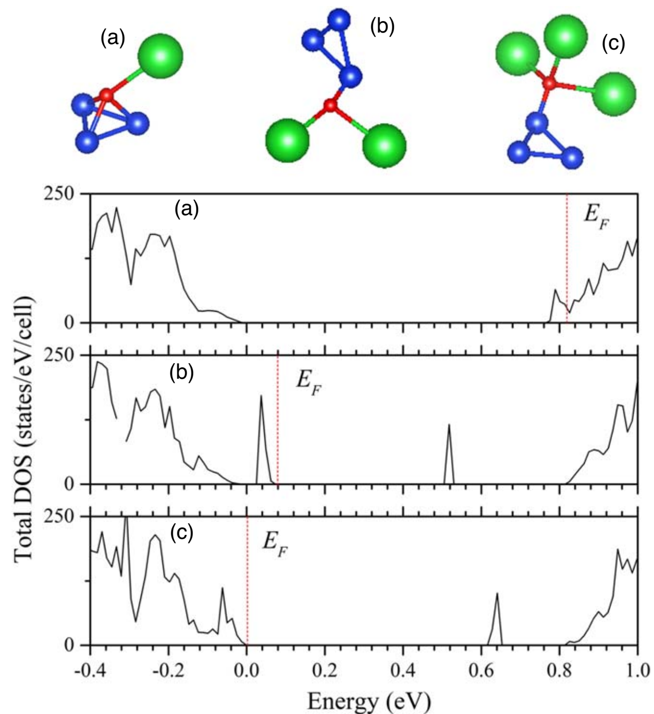

Fig. 6. (Color online) The total density of states of $BaSi_2$ with an O atom as a substitution impurity. The vertical dashed line indicates the Fermi level (E_F). Atomic configurations in the vicinity of the O atom are also shown. The large green spheres indicate Ba atoms, medium blue and red spheres stand for Si and O atoms, respectively.

distances three distinct cases were detected for an O atom in $BaSi_2$ acting both as a substitutional and interstitial impurity (see Figs. 6 and 7). In the case of the substitutional impurity localized states appear in the gap which can be filled and located close to (or even merged with) the conduction band [n-type conductivity, Fig. 6(a)] or to the valence band [a deep donor level, Fig. 6 (b)]. In addition, the empty states are also formed in the gap [acting as a trap Fig. 6(b) or deep acceptor level Fig. 6(c)]. The latter cases [namely (b) and (c)] are found to be

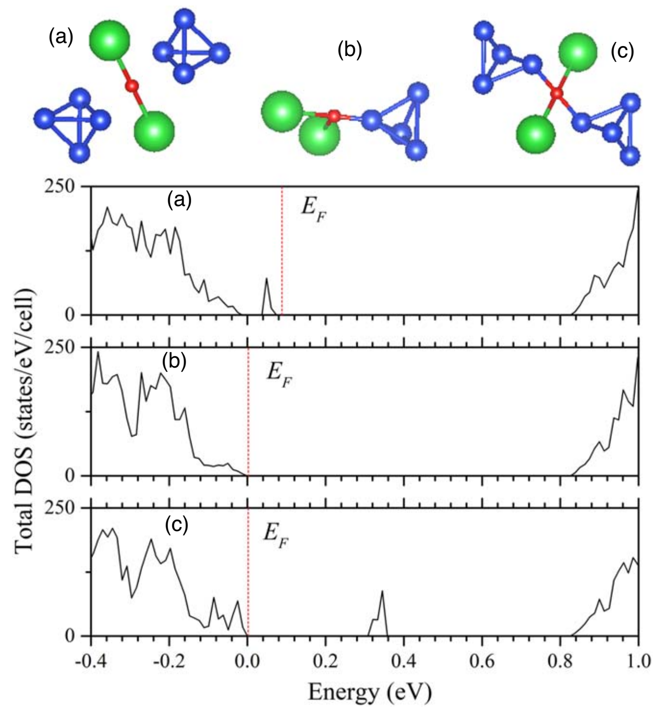

Fig. 7. (Color online) The total density of states of $BaSi_2$ with an O atom as an interstitial impurity. The vertical dashed line indicates the Fermi level (E_F). Atomic configurations in the vicinity of the O atom are also shown. The large green spheres indicate Ba atoms, medium blue and red spheres stand for Si and O atoms, respectively.

rather close in the total energy ($\sim$0.2 eV cell^{-1}) whereas the case (a) is higher by $\sim$2.0 eV cell^{-1} indicating that an O atom prefers to have only one Si atom as the first neighbor. The localized states can be seen for an interstitial O atom: the filled state close to the valence band [a deep donor level, Fig. 7(a)] and the empty state near the middle of the gap [a trap, Fig. 7(c)]. It is also possible that an interstitial O atom does not cause the formation of a localized state at all [Figs. 7(b)] and this case (b) is more energetically preferable (by $\sim$2.0 eV cell^{-1}) with respect to the other two cases (a) and (c) also following the same tendency to have only one Si–O bond. Since intrinsic $BaSi_2$ usually displays n-type conductivity,[74] it is evident that doping O atoms into $BaSi_2$ should not affect the conductivity type.

Even though doping of $BaSi_2$ by B atoms (acting as a substitution impurity) leads to the clear p-type conductivity,[75] the observed n-type conductivity with a sizable concentration of O (1.5×10^{21} cm^{-3}) and B (3×10^{18} cm^{-3}) atoms seems unreasonable. However, it is possible for the n-type conductivity of B- and O-doped $BaSi_2$ to appear only in the cases when both B and O atoms are the substitution impurity in the same Si_4 tetrahedron. Here, a half-filled state is formed in the gap close to the bottom of the conduction band [acting as a donor Fig. 8(a)] or this half-filled state is merged with (or very close to) the conduction band [Fig. 8(b)]. The case (a) is lower in the total energy (by $\sim$2.0 eV cell^{-1}) with respect to the case (b). Any variant when one of the impurity atoms is a substitution impurity whereas another one occupies an interstitial position [Fig. 8(c)] results in a half-filled state lying between the middle of the gap (trap) and the top of the valence band (acceptor level). In terms of the formation energy, the cases with O and B atoms acting as substitutional impurities are

© 2022 The Japan Society of Applied Physics

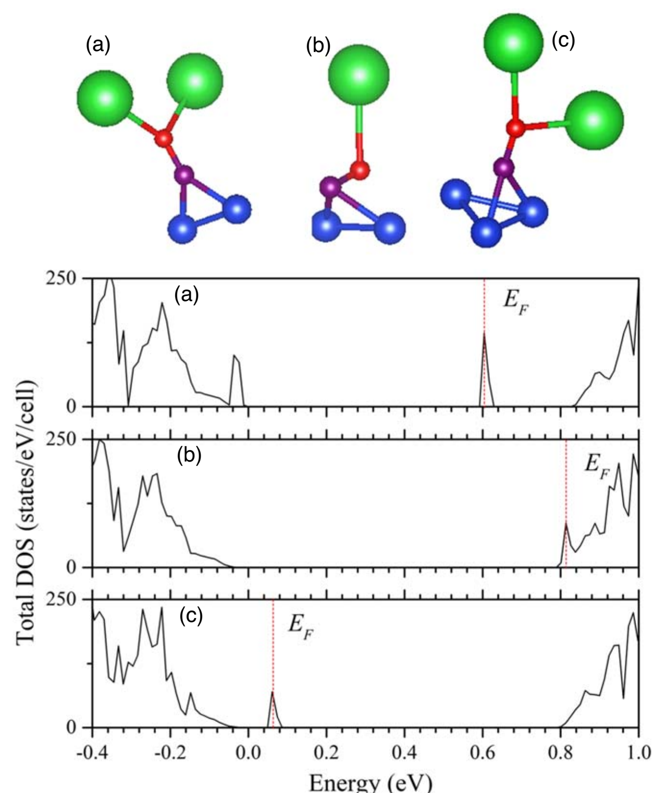

Fig. 8. (Color online) The total density of states of $BaSi_2$ doped with O and B atoms: (a) and (b) both O and B atoms as a substitution impurity in the same Si_4 tetrahedron, (c) one of the impurity atoms is a substitution impurity whereas another one occupies an interstitial position. Zero at the energy scale corresponds to the top of the valence band. The vertical dashed line indicates the Fermi level (E_F). Atomic configurations in the vicinity of the O atom are also shown. The large green spheres indicate Ba atoms, medium blue spheres stand for Si atoms and small red and magenta spheres are O and B atoms, respectively.

slightly energetically favorable (0.2 eV $cell^{-1}$) than the cases where they are substitutional and interstitial impurities simultaneously. On the basis of the above discussions, it is considered that the as-deposited B-doped $BaSi_2$ films exhibited n-type conductivity and became p-type by the post-annealing at 1000 °C because of the following reasons. In the as-deposited B-doped $BaSi_2$, the B and O atoms were positioned in the same Si_4 tetrahedron in terms of formation energy, as shown in Fig. 8(a), indicating n-type conductivity. By the high-temperature annealing, O atoms migrated to interstitial sites, while B atoms remained at the substitutional sites, creating the situation in Fig. 8(c) and thus the p-type $BaSi_2$ formed. How to reduce the O atoms in the sputter-deposited $BaSi_2$ films is a future challenge.

4. Conclusion

In this study, B-doped $BaSi_2$ films were fabricated by simultaneous sputtering $BaSi_2$ target, Ba target, and B-doped Si target, followed by post-annealing at 900 °C and 1000 °C. The diffraction peaks obtained by GI-XRD and Raman spectra showed that B-doped polycrystalline $BaSi_2$ films were fabricated on Si substrates. The as-grown sample and the annealed sample at 900 °C showed n-type conductivity, while the annealed sample showed p-type conductivity. The reason for the n-type conductivity of the as-deposited sample is thought to be that the sample fabricated by sputtering has excess O, and the B and excess O replace the Si in the same Si tetrahedron composed of $BaSi_2$.

Acknowledgments

This work was financially supported in part by JSPS KAKENHI (Grant No. JP18H03767 and JP21H04548). A part of this work was supported by "Advanced Research Infrastructure for Materials and Nanotechnology in Japan (ARIM)" of the Ministry of Education, Culture, Sports, Science and Technology (No. JPMXP1222BA002). D. B. Migas acknowledges the support of the MEPhI Program Priority 2030.

1) K. Yoshikawa et al., Nat. Energy **2**, 17032 (2017).
2) T. Feurer et al., Prog. Photovol. **25**, 645 (2017).
3) J. Ramanujam, D. M. Bishop, T. K. Todorov, O. Gunawan, J. Rath, R. Nekovei, E. Artegiani, and A. Romeo, Prog. Mater. Sci. **110**, 100619 (2020).
4) M. Kumar, A. Dubey, N. Adhikari, S. Venkatesan, and Q. Q. Qiao, Energy Environ. Sci. **8**, 3134 (2015).
5) K. Pal, P. Singh, A. Bhaduri, and K. B. Thapa, Sol. Energy Mater. Sol. Cells **196**, 138 (2019).
6) M. Powalla, S. Paetel, E. Ahiswede, R. Wuerz, C. D. Wessendorf, and T. M. Friedlmeier, Appl. Phys. Rev. **5**, 041602 (2018).
7) M. Barbato et al., J. Phys. D: Appl. Phys. **54**, 333002 (2021).
8) G. D. Niu, X. D. Guo, and L. D. Wang, J. Mater. Chemistry A **3**, 8970 (2015).
9) T. Leijtens, G. E. Eperon, N. K. Noel, S. N. Habisreutinger, A. Petrozza, and H. J. Snaith, Adv. Energy Mater. **5**, 1500963 (2015).
10) D. Wang, M. Wright, N. K. Elumaiai, and A. Uddin, Solar Ener. Mater. Sol. Cells **147**, 255 (2016).
11) T. A. Berhe, W. N. Su, C. H. Chen, C. J. Pan, J. H. Cheng, H. M. Chen, M. C. Tsai, L. Y. Chen, A. A. Dubale, and B. J. Hwang, Energy Environ. Sci. **9**, 323 (2016).
12) N. G. Park and K. Zhu, Nat. Rev. Mater. **5**, 333 (2020).
13) T. Suemasu, Jpn. J. Appl. Phys. **54**, 07JA01 (2015).
14) T. Suemasu and N. Usami, J. Phys. D **50**, 023001 (2017).
15) M. Kumar, N. Umezawa, and M. Imai, Jpn. J. Appl. Phys. **59**, SF0803 (2020).
16) T. Suemasu and D. B. Migas, Phys. Status Solidi a **219**, 2100593 (2022).
17) K. Morita, Y. Inomata, and T. Suemasu, Thin Solid Films **508**, 363 (2006).
18) W. Shockley and H. J. Queisser, J. Appl. Phys. **32**, 510 (1961).
19) K. Toh, T. Saito, and T. Suemasu, Jpn. J. Appl. Phys. **50**, 068001 (2011).
20) D. B. Migas, V. L. Shaposhnikov, and V. E. Borisenko, Phys. Status Solidi B **244**, 2611 (2007).
21) M. Kumar, N. Umezawa, and M. Imai, Appl. Phys. Express **7**, 071203 (2014).
22) M. Kumar, N. Umezawa, W. Zhou, and M. Imai, J. Mater. Chem. A **5**, 25293 (2017).
23) K. Takahashi, Y. Nakagawa, K. O. Hara, Y. Kurokawa, and N. Usami, Jpn. J. Appl. Phys. **56**, 05DB04 (2017).
24) Q. R. Deng, H. Chen, H. Liao, L. Chen, G. M. Wang, S. G. Wang, and Y. L. Shen, J. Phys. D: Appl. Phys. **52**, 075501 (2018).
25) L. Chen, H. Chen, Q. R. Deng, G. M. Wang, and S. G. Wang, Solid. State. Electron. **149**, 46 (2018).
26) M. M. A. Moon, M. H. Ali, M. F. Rahman, A. Kuddus, J. Hossain, and A. M. Ismail, Phys. Scr. **95**, 035506 (2020).
27) K. O. Hara, J. Phys. Chem. C **125**, 24310 (2021).
28) H. Liao, C. A. M. Cheng, G. M. Wang, S. G. Wang, P. F. Li, and Q. R. Deng, Mod. Phys. Lett. B **35**, 2150521 (2021).
29) S. Yachi, R. Takabe, H. Takeuchi, K. Toko, and T. Suemasu, Appl. Phys. Lett. **109**, 072103 (2016).
30) T. Deng, T. Sato, Z. Xu, R. Takabe, S. Yachi, Y. Yamashita, K. Toko, and T. Suemasu, Appl. Phys. Express **11**, 062301 (2018).
31) T. Nemoto, S. Aonuki, R. Koitabashi, Y. Yamashita, M. Mesuda, K. Toko, and T. Suemasu, Appl. Phys. Express **14**, 051010 (2021).
32) M. Fujiwara, K. Takahashi, Y. Nakagawa, K. Gotoh, T. Itoh, Y. Kurokawa, and N. Usami, AIP Adv. **12**, 045115 (2022).
33) K. Kodama, Y. Yamashita, K. Toko, and T. Suemasu, Appl. Phys. Express **12**, 041005 (2019).
34) Y. Yamashita, C. M. R. Tobon, R. Santbergen, M. Zeman, O. Isabella, and T. Suemasu, Sol. Ener. Mater. Sol. Cells **230**, 111181 (2021).
35) Y. Yamashita, K. Takayanagi, K. Gotoh, K. Toko, N. Usami, and T. Suemasu, ACS Appl. Mater. Interfaces **14**, 13828 (2022).
36) K. O. Hara, K. Arimoto, J. Yamanaka, and K. Nakagawa, Jpn. J. Appl. Phys. **58**, SBBF01 (2019).

 © 2022 The Japan Society of Applied Physics

37) T. Yoshino, Y. Nakagawa, Y. Kimura, M. Fujiwara, Y. Kurokawa, and N. Usami, Jpn. J. Appl. Phys. **59**, SFFA10 (2020).
38) Y. Kimura, M. Fujiwara, Y. Nakagawa, K. Gotoh, Y. Kurokawa, and N. Usami, Jpn. J. Appl. Phys. **59**, SFFA05 (2020).
39) K. O. Hara, K. Arimoto, J. Yamanaka, and K. Nakagawa, Jpn. J. Appl. Phys. **59**, SFFA02 (2020).
40) K. O. Hara, S. Takizawa, J. Yamanaka, N. Usami, and K. Arimoto, Mater. Sci. Semicond. Process. **113**, 105044 (2020).
41) K. O. Hara, C. Yamamoto, J. Yamanaka, and K. Arimoto, Mater. Adv. **2**, 6713 (2021).
42) T. Suemasu, K. O. Hara, H. Udono, and M. Imai, J. Appl. Phys. **131**, 191101 (2022).
43) S. Matsuno, R. Takabe, S. Yokoyama, K. Toko, M. Mesuda, H. Kuramochi, and T. Suemasu, Appl. Phys. Express **11**, 071401 (2018).
44) T. Nemoto, R. Koitabashi, M. Mesuda, K. Toko, and T. Suemasu, Appl. Phys. Express **13**, 085511 (2020).
45) R. Koitabashi, T. Nemoto, Y. Yamashita, M. Mesuda, K. Toko, and T. Suemasu, J. Phys. D: Appl. Phys. **54**, 135106 (2021).
46) R. Dui, F. Li, K. Yang, Q. Li, W. Du, Y. Zhang, and T. Suemasu, Appl. Phys. Express **14**, 065501 (2021).
47) R. Koitabashi, K. Kido, H. Hasebe, M. Mesuda, K. Toko, and T. Suemasu, AIP Adv. **12**, 045120 (2022).
48) R. Koitabashi, K. Kido, H. Hasebe, Y. Yamashita, K. Toko, M. Mesuda, and T. Suemasu, Appl. Phys. Express **15**, 025502 (2022).
49) K. Kido, R. Koitabashi, T. Ishiyama, H. Hasebe, M. Mesuda, K. Toko, and T. Suemasu, Thin Solid Films **758**, 139426 (2022).
50) M. A. Khan, K. O. Hara, W. Du, M. Baba, K. Nakamura, M. Suzuno, K. Toko, N. Usami, and T. Suemasu, Appl. Phys. Lett. **102**, 112107 (2013).
51) M. A. Khan, K. Nakamura, W. Du, K. Toko, N. Usami, and T. Suemasu, Appl. Phys. Lett. **104**, 252104 (2014).
52) K. Takahashi, Y. Nakagawa, K. O. Hara, I. Takahashi, Y. Kurokawa, and N. Usami, MRS Adv. **3**, 1435 (2018).
53) Y. Nakagawa, K. Takahashi, M. Fujiwara, K. O. Hara, K. Gotoh, Y. Kurokawa, T. Itoh, T. Suemasu, and N. Usami, Jpn. J. Appl. Phys. **60**, 105503 (2021).
54) K. O. Hara, N. Usami, Y. Hoshi, Y. Shiraki, M. Suzuno, K. Toko, and T. Suemasu, Jpn. J. Appl. Phys. **50**, 121202 (2011).
55) S. Aonuki, K. Toko, and T. Suemasu, APAC SilicideSun-p-O12, online July 31 (2022).
56) C. Agashe, O. Kluth, J. Hüpkes, U. Zastrow, and B. Rech, J. Appl. Phys. **95**, 1911 (2004).
57) A. Mosbah and M. S. Aida, J. Alloys Compd. **515**, 149 (2012).
58) A. Spadoni and M. L. Addonizio, Thin Solid Films **589**, 514 (2015).
59) D. C. Look, Appl. Phys. Lett. **85**, 5269 (2004).
60) R. Takabe, H. Takeuchi, W. Du, K. Ito, K. Toko, S. Ueda, A. Kimura, and T. Suemasu, J. Appl. Phys. **119**, 165304 (2016).
61) T. Suhara, K. Murata, A. Navabi, K. O. Hara, Y. Nakagawa, C. T. Trinh, Y. Kurokawa, T. Suemasu, K. L. Wang, and N. Usami, Jpn. J. Appl. Phys. **56**, 05DB05 (2017).
62) G. Kresse and J. Hafner, Phys. Rev. B **49**, 14251 (1994).
63) G. Kresse and J. Furthmüller, Phys. Rev. B **54**, 11169 (1996).
64) G. Kresse and D. Joubert, Phys. Rev. B **59**, 1758 (1999).
65) J. Evers, J. Solid State Chem. **32**, 77 (1980).
66) J. P. Perdew, K. Burke, and M. Ernzerhof, Phys. Rev. Lett. **77**, 3865 (1996).
67) H. Hoshida, T. Suemasu, and Y. Terai, Defect and Diffusion Forum **386**, 43 (2018).
68) Y. Haku, S. Aonuki, Y. Yamashita, K. Toko, and T. Suemasu, Appl. Phys. Express **14**, 021003 (2021).
69) M. Imai, Jpn. J. Appl. Phys. **50**, 101801 (2011).
70) S. Narita, Y. Yamashita, S. Aonuki, N. Saitoh, K. Toko, and T. Suemasu, J. Cryst. Growth **578**, 126429 (2022).
71) Y. Imai and A. Watanabe, Intermetallics **15**, 1291 (2007).
72) S. Sugiyama, Y. Yamashita, K. Toko, and T. Suemasu, Jpn. J. Appl. Phys. **59**, SFFA04 (2020).
73) D. A. Shohonov, D. B. Migas, A. B. Filonov, V. E. Borisenko, R. Takabe, and T. Suemasu, Thin Solid Films **686**, 137436 (2019).
74) T. Deng, T. Suemasu, D. A. Shohonov, I. S. Samusevich, A. B. Filonov, D. B. Migas, and V. E. Borisenko, Thin Solid Films **661**, 7 (2018).
75) Z. Xu et al., J. Appl. Phys. **127**, 233104 (2020).

© 2022 The Japan Society of Applied Physics